nuclear fusion
IAEA

PAPER • OPEN ACCESS

L to H mode transition: parametric dependencies of the temperature threshold

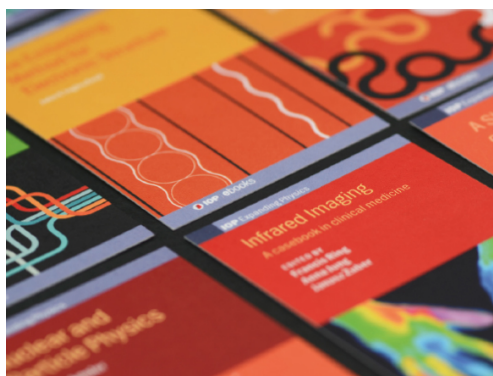To cite this article: C. Bourdelle *et al* 2015 *Nucl. Fusion* **55** 073015

View the article online for updates and enhancements.

Related content

Recent citations

L to H mode transition: parametric dependencies of the temperature threshold

C. Bourdelle[1], L. Chôné[1,2], N. Fedorczak[1], X. Garbet[1], P. Beyer[2], J. Citrin[1,3], E. Delabie[4], G. Dif-Pradalier[1], G. Fuhr[2], A. Loarte[5], C.F. Maggi[6], F. Militello[6], Y. Sarazin[1], L. Vermare[7] and JET Contributors[a]

[1] CEA, IRFM, F-13108 Saint-Paul-lez-Durance, France

[2] Aix-Marseille Université, CNRS, PIIM UMR 7345, 13397 Marseille Cedex 20, France

[3] FOM Institute DIFFER-Dutch Institute for Fundamental Energy Research, Trilateral Euregio Cluster, PO Box 1207, 3430 BE Nieuwegein, The Netherlands

[4] Oak Ridge National Laboratory, Oak Ridge, Tennessee 37831, USA

[5] ITER Organization, Route de Vinon sur Verdon, 13115 St Paul Lez Durance, France

[6] Culham Centre for Fusion Energy, Abingdon, UK

[7] Laboratoire de Physique des Plasmas, Ecole Polytechnique, 91128, Palaiseau, CEDEX, France

E-mail: Clarisse.bourdelle@cea.fr

Abstract

The L to H mode transition occurs at a critical power which depends on various parameters, such as the magnetic field, the density, etc. Experimental evidence on various tokamaks (JET, ASDEX-Upgrade, DIII-D, Alcator C-Mod) points towards the existence of a critical temperature characterizing the transition. This criterion for the L-H transition is local and is therefore easier to be compared to theoretical approaches. In order to shed light on the mechanisms of the transition, simple theoretical ideas are used to derive a temperature threshold (T_{th}). They are based on the stabilization of the underlying turbulence by a mean radial electric field shear. The nature of the turbulence varies as the collisionality decreases, from resistive ballooning modes to ion temperature gradient and trapped electron modes. The obtained parametric dependencies of the derived T_{th} are tested versus magnetic field, density, effective charge. Various robust experimental observations are reproduced, in particular T_{th} increases with magnetic field B and increases with density below the density roll-over observed on the power threshold.

Keywords: plasma physics, L H transition, tokamak

(Some figures may appear in colour only in the online journal)

1. Introduction

The L to H mode transition occurs at a critical power which depends on various parameters, such as the magnetic field, the density, etc [1–3]. This global approach of the transition is difficult to compare to theoretical approaches based on local mechanisms. Therefore, various attempts to define the L to H transition in terms of local parameters have been carried out in various machines. The most recent was done on 67 JET pulses using a neural network classification technique [4]. A temperature threshold, T_{th}, increasing with large magnetic field B, decreasing with larger density n and weakly decreasing with safety factor q is reported. The trends are consistent with former works done in ASDEX Upgrade [5], Alcator C-Mod [6], DIII-D [7], etc. These scaling laws have been derived on the electron temperature, which has been historically better diagnosed than the ion temperature. No cross-machine scaling of the temperature threshold is presently available, nonetheless, some common features emerge, such as an increase with larger magnetic field and a weaker dependence on density than the one reported for the power threshold, P_{th}. The parametric dependencies of the power and of the temperature are expected to differ [1].

In order to shed light on the mechanisms responsible for the transition above a critical temperature, the combination of two popular ideas is proposed. Namely, the role of the L mode edge unstable Resistive Ballooning Modes [8] and the stabilization by mean radial electric field, E_r, shear [9] are combined. The principle is to identify two times,

one characterizing the turbulence and one characterizing the mean flow. The assumption made is that the transition in H mode occurs when the shortest of the two times is the one characterizing the mean E_r shear. Many L to H transition models are based on this assumption, see [10] for a review. Experimentally, it has long been seen that E_r was a key player of the transition, read [9] for a review. The interplay between turbulence and E_r shearing has been proposed long ago by various authors to explain the transition, see [10, 11] for complete references. This interpretation has been opposed to the Resistive Ballooning Mode mechanism proposed by [8] and others (see [10] for more complete references). In those works, RBM were proposed to be stabilized by increased pressure gradients due to larger MHD parameter α. In the process described in this present work, RBM are stabilized by increased T leading to reduced collisonality, until ITG-TEM take over. Experimental investigation of TCV L mode plasmas shows that the edge region exhibits a different transport response than the core [12]. On the theory/modeling side, RBM have been recently found to be linearly unstable in gyrokinetic modeling using parameters of DIII-D and Tore Supra L mode edges [13] as well as parameters of JET-ILW pedestal forming region prior to the H mode onset [14]. In this later case, the RBM growth rate reaches a minimum for temperatures in the range at which the transition into H mode occurs. The presence of unstable RBM has been shown to be in qualitative agreement with a larger power threshold obtained at larger Z_{eff}, see [14, 15] and references therein. On the other hand, recent experimental measurements still point strongly towards a key role of E_r [15–19].

Based on this theoretical approach, an analytical formula for the turbulence growth rate, γ_{turb}, and another analytical formula for the mean E_r shearing rate, γ_E, are derived. The ratio of the two competing times, γ_{turb}/γ_E decreases for increasing T. It reaches a critical value below which the transition into H mode is assumed. A temperature corresponds to the critical value of γ_{turb}/γ_E, it is the temperature threshold T_{th}. If one of the other parameters such as n, B, Z_{eff}, etc is modified, T_{th} varies too. Hence, with this model, the parametric dependencies of T_{th} can be investigated. The temperature threshold is tested against magnetic field and other parameters reported to have a significant impact [4–6, 20]. But also, parameters known to impact the power threshold will be tested such as the effective charge Z_{eff} proposed in [2]; the isotopic effect showing that the threshold is higher in H than in D [1, 21].

In sections 2 and 3, the theoretical approach is detailed. First the choice for the turbulence growth is justified and analytically derived. Then the choice for the mean E_r shear is explained and its analytical derivation detailed. In section 4, the ratio of both times is studied, and temperature threshold dependencies analyzed. In particular, it is shown how the temperature threshold varies with parameters such as B, n, Z_{eff}, the isotopic effect and He versus D. It is demonstrated that the stabilization trends are in qualitative agreement with the reported experimental tendencies of the threshold. Finally, the weaknesses and strengths of the approach are discussed and conclusions are drawn in section 5.

2. The turbulence time scale: $1/\gamma_{turb}$

In this section, before deriving analytically the turbulence growth rate, some experimental observations are reported on the role of Z_{eff}. In some cases, an increased Z_{eff} leads to higher power threshold P_{th} which is suggestive of resistivity driven unstable modes at play. Indeed, in JET-ILW, for parameters of the pedestal forming region prior to the transition, RBM have been found to be linearly unstable [14]. Therefore, both the RBM growth rates, γ_{RBM}, and the ITG-TEM growth rates, $\gamma_{ITG,TEM}$, will be derived analytically; γ_{turb} being the maximum of γ_{RBM} and $\gamma_{ITG,TEM}$.

2.1. On the Z_{eff} impact on the L to H transition threshold

Recent observations of the impact of the ITER Like Wall (ILW) in JET show a L to H mode power threshold, P_{L-H} reduced by $\simeq 40\%$ in JET-ILW with respect to similar experiments in C wall [15]. This reduction is observed in the high density branch. The experiments were carried out with slow power ramps and matched plasma shapes, divertor configurations and (I_p, B_T) pairs. Despite different divertor configurations, geometries and wall materials a similar reduction in P_{L-H} is reported in ASDEX Upgrade with full W wall [22, 23]. A common feature of both JET and ASDEX Upgrade is a significant reduction of Z_{eff} when switching from C walls to metallic ones.

Numerous past results have shown that divertor geometry and plasma shape strongly impact the power threshold. Note that the power threshold is the net power through the separatrix: $P_{th} = P_{abs} - P_{rad,bulk}$, $P_{rad,bulk}$ being the radiated power from the bulk plasma and P_{abs} the power absorbed by the bulk plasma. The L-H power threshold has been found to be lower by 20 to 35% with increased divertor closure in JET-C [24, 25] and in JT-60U [26]. In recent Alcator C-Mod experiments, the slot divertor configuration is associated with a lower power threshold than the vertical target configuration [27]. For both JET-C and JT60-U, during L mode phases, an increased divertor closure is associated with lower Z_{eff}. In Alcator C-Mod slot divertor, a lower radiated power from the bulk plasma [27] is reported. In DIII-D a lower X point height leads to a lower threshold [28]. A similar X-point height impact is also reported for JET-C [29]. In the DIII-D case, a lower D_α in the main chamber is reported as the X point height is decreased. Such trend could be linked to modified Z_{eff}. Indeed, the plasma contamination can respond to reduced main chamber neutrals [24, 30], modified divertor screening [31], divertor and wall temperatures [32], distance from the LCFS to the wall, SOL parallel flows, etc. Therefore, a link between these various results could be that, through a modified divertor geometry and/or plasma shape, a reduced contamination, hence Z_{eff}, favors a lower L-H power threshold. Indeed, in 2004, an ITPA scaling law for P_{th} proposed a dependence with Z_{eff} [2] based on JT60-U observations at a given density and the limited information on Z_{eff} from various machines present in the data base at that time. This scaling law has been recently shown to reduce the spread of JET-ILW and JET-C data points compared to the ITPA 2008 scaling law without Z_{eff} [33].

The link between a modified plasma shape and a modified Z_{eff} has been tested on recent JET-ILW data where five

different configurations have been explored at 2.4 T / 2.0 MA and constant density. Three configurations kept the upper triangularity (δ_U) fixed to high values while moving the strike point positions; and two configurations kept the upper triangularity to a lower value while modifying the lower triangularity (δ_L) [15]. A reduction of P_{th} (from 3 MW down to 1.5 MW) at constant density is observed to correlate better with a reduction of Z_{eff}, rather than with modified δ_U and δ_L [15]. Although Z_{eff} is likely a player, other effects such as the X point configuration (single null, double null, $B \times \nabla B$ drift direction) have been long demonstrated to be other key players [1, 34].

The fact that lower Z_{eff} seem to ease the L to H transition is suggestive of a key role of resistivity in the turbulence drive. To check this hypothesis, JET-ILW data prior to the L to H mode transition has been analyzed by the linear gyrokinetic code Gene [35] as reported in [14]. The temperature was scanned. At low temperature, corresponding to the temperature range where the transition is obtained, Resistive Ballooning Modes are found linearly unstable. As the temperature is increased, i.e. as the resistivity is reduced, RBM are stabilized. When increasing further the temperature, ITG-TEM take over and are further destabilized as the temperature is increased due to more active TEM at lower collisionality. The competition between stabilized RBM and destabilized ITG-TEM leads to a growth rate which is minimum at a given temperature. Interestingly, the temperature range of this minimum is of the order of the experimentally measured temperature at which the transition into H mode occurs. The second stability limit, due to large MHD parameter α [36, 37], occurs at temperatures well above the experimental range as illustrated in appendix A. This stabilization mechanism cannot be responsible for the transition into H mode. Therefore, as the T is increased, the transition into H mode is expected to be facilitated when the RBM growth rates are reduced, before the ITG-TEM branch takes over. For a larger Z_{eff}, the RBM growth rates increase, hence one expects higher threshold for higher Z_{eff}. This observation is in qualitative agreement with the previously reported experimental observations. Therefore, in the following, an analytical model is built to reproduce the competition between the stabilized RBM and the destabilized ITG-TEM as the temperature is increased.

2.2. Analytically derived turbulence growth rate

The competition between RBM and ITG-TEM is modeled analytically. The turbulence growth rate γ_{turb} will be the maximum between γ_{RBM} and $\gamma_{ITG-TEM}$. The obtained growth rates will be compared to Gene's results.

2.2.1. Analytical RBM modeling.
The analytical derivation of the RBM growth rate is based on the derivation detailed in [13] where the fluid equations are re-derived starting from a kinetic variational formalism proposed in [38]. The $s - \alpha$ magnetic equilibrium is used. The dispersion relation allows to obtain both w_{RBM}, characterizing the eigenfunction width, and the growth rate, γ_{RBM}, characterizing the eigenvalue.

In the previous derivation [13], one type of ions was assumed with $n_e = n_i = n$ as well as $T_e = T_i = T$. In the following, these approximations are relaxed, with $\tau = T_i/T_e$

and $n_e = \sum_s Z_s n_s$, Z_s and n_s being respectively the charge number and the density of the ion species 's'. Moreover, the magnetic shear s and the MHD α parameter contributions to the curvature and grad-B drift frequency, $n\omega_D$, are included. Based on [39], $n\omega_D$ for deeply trapped particles and averaged over the pitch angle becomes:

$$n\omega_D = \frac{k_\theta T_e}{eB}\frac{1}{R}0.2(1 + 1.9(s - \alpha)) \tag{1}$$

The RBM dispersion relation is then derived in the fluid limit. The electrostatic case is assumed. This assumption can be justified a posteriori by comparing the terms of the Ohm's law $\eta J_\| = -i\left(\omega A_\| - k_\|\phi\right)$ using that $\nabla_\perp^2 A_\| = -\mu_0 J_\|$. The electrostatic limit is adequate if $\gamma \ll \frac{\eta}{\mu_0}k_\perp^2$. As detailed in the appendix B, for the parameters used later and using the derivation detailed with $k_\perp = \frac{2\pi}{w_{RBM}}$, one finds that $\gamma = \gamma_{RBM}$ is, at most, two orders of magnitude lower than $\frac{\eta}{\mu_0}k_\perp^2$. As well, in [13], the linear gyrokinetic analysis using Gene has shown that for edge parameters, the electrostatic results almost perfectly overlap with the electromagnetic linear growth rates and frequencies.

The low wave number limit is taken as well as the usual fluid ordering $\omega >> n\omega_D$, where $\omega = \omega_r + i\gamma$ ω_r is the mode frequency and γ its growth rate. In the strongly resistive limit, where the collisionality, ν, is such that: $\nu >> \omega, n\omega_D, k_\|v_\|$ (with $k_\|v_\|$ the transit frequency and $\frac{1}{\nu} = 3(2\pi)^{3/2}\frac{\epsilon_0^2 m_e^{1/2}T^{3/2}}{n_e Z_{eff} e^4 \ln \Lambda}$), the dispersion relation then becomes:

$$(1 + \frac{\tau}{\bar{Z}})\langle n\omega^* n\omega_D\rangle + \frac{i}{3}\left\langle \frac{\omega - n\omega^*}{\nu\left(\frac{T}{E}\right)^{3/2}}k_\|^2 v_\|^2\right\rangle$$
$$+ \frac{1}{2}\sum_s \frac{Z_s^2 n_s}{n_e}\frac{1}{\tau}\left\langle k_\perp^2\rho_s^2\omega\left(\omega + \frac{\tau}{Z_s}n\omega^*\right)\right\rangle = 0 \tag{2}$$

with $\bar{Z} = \frac{n_e}{\sum_s n_s}$, $n\omega^*$ the diamagnetic frequency such that $n\omega^* = n\omega_e^* = -\frac{k_\theta T}{eB}\left(\frac{\nabla n}{n} + \left(\frac{E}{T} - \frac{3}{2}\right)\frac{\nabla T}{T}\right)$, E is the total energy, all the temperatures and densities are taken homothetic $\frac{\nabla T}{T} = \frac{\nabla T_e}{T_e} = \frac{\nabla T_i}{T_i}$ and $\frac{\nabla n}{n} = \frac{\nabla n_e}{n_e} = \frac{\nabla n_s}{n_s}$ for all ion species s, $v_\|$ the velocity along the magnetic field line, $k_\|$ the wave vector along the magnetic field line, ϕ the electrostatic potential, $A_\|$ the vector potential, ω the frequency of the mode, and ρ_s the Larmor radius of the ion species s such that $\rho_s = \rho\sqrt{2\tau}\sqrt{A_s}/Z_s$ with $\rho = \frac{\sqrt{T_e m_D}}{eB}$. For greater details on the derivation of this dispersion relation see [13].

The first term drives the instability as for usual interchange modes (pressure gradient aligned with curvature). The second term is related to the Ohm's law and is stabilizing. This term is responsible for the resistive character of the modes. Indeed it is smaller for larger collisionality (i.e. resistivity). The third term is related to ion inertia (Finite Larmor Radius and polarization effects), and is also stabilizing. The competition between these three effects leads to the Resistive Ballooning Mode in the strongly resistive fluid limit. Since $k_\perp^2 = -\frac{d^2}{dx^2} + k_\theta^2$ and near a resonant surface, $k_\|v_\| \simeq \dot{k_\|}xv_\|$ ($\dot{k_\|} = \frac{k_\theta}{L_s}$, where $L_s = qR/s$ is the shear length, x is the distance to the resonant surface), the electrostatic potential is solution of a second order differential equation, such that: $\phi \propto e^{-x^2/w^2}$. Equation (2) can be split in two parts, one made of terms proportional to x^2 and the other of terms independent of x. From the first part, the mode width, w_{RBM}, is determined by the equilibrium between

the perpendicular dynamics fixed by the finite Larmor radius effect and the parallel dynamics constrained by the resistive term as follows:

$$\left(\frac{w_{\text{RBM}}}{\rho}\right)^2 \simeq \frac{\sqrt{\tau}}{\sqrt{\bar{C}}} \frac{\sqrt{6\nu\gamma_{\text{RBM}}}}{\omega_{te}} \tag{3}$$

with $\bar{C} = \frac{n_e}{\sum_s A_s n_s}$ and $\omega_{te} = \dot{k}_\parallel \rho_D v_{\text{the}}$ is the electron transit frequency (v_{the} being the electron thermal velocity).

The second part is such that the interchange drive with the ion inertia term provides a relationship between the mode width and the growth rate γ (in the limit $\omega \gg \omega^*$) such that:

$$\gamma_{\text{RBM}} = \gamma_I k_\theta w_{\text{RBM}} \frac{\sqrt{1 + \frac{\tau}{\bar{Z}}}}{\sqrt{2/\bar{C}}} \tag{4}$$

where $\gamma_I = \frac{c_s}{\sqrt{RL_p}} \sqrt{0.2(1 + 1.9(s - \alpha))}$ is the interchange growth rate. $c_s = \sqrt{T_e/m_D}$ is a thermal velocity. Note that, if $(1 + 1.9(s - \alpha)) < 0$ then γ_I is forced to zero since in such case there is no drive for the interchange instability.

Combining equations (3) and (4) yield to the following expression for the RBM growth rate:

$$\frac{\gamma_{\text{RBM}}}{\gamma_I} \simeq (\tau \bar{C})^{1/3} (1 + \tau/\bar{Z})^{2/3} (k_\theta \rho)^{4/3} \left(\frac{6\gamma_I \nu}{\omega_{te}^2}\right)^{1/3} \tag{5}$$

The radial scale of the mode becomes:

$$\frac{w_{\text{RBM}}}{\rho} \simeq \frac{\sqrt{2}}{\sqrt{\bar{C}}} \tau^{1/3} (1 + \tau/\bar{Z})^{1/6} (k_\theta \rho)^{1/3} \left(\frac{6\gamma_I \nu}{\omega_{te}^2}\right)^{1/3} \tag{6}$$

From equation (5), it is clear that RBM are destabilized if the product of the interchange growth rate with the collisionality, $\gamma_I \nu$, is large compared to the square of the electron parallel transit frequency, ω_{te}^2. Therefore larger collisionality is destabilizing as well as larger normalized density and temperature gradients. Higher magnetic shear, s, is stabilizing through larger ω_{te}, higher q is destabilizing through lower ω_{te}.

At fixed $k_\theta \rho$ one obtains that γ_{RBM} is a function of τ, T_e, n_e, q, s, L_p, R, A_s, Z_s and Z_{eff}.

2.2.2. Analytical derivation of the ITG-TEM branch.
As the temperature is scanned, it was reported in [14] that for lower collisionalities, the ITG-TEM branch takes over RBM. To account analytically for this competition between these two types of modes, an analytical model for ITG-TEM is proposed. It is derived in the fluid limit where the gyrokinetic equation is developed assuming that the frequency of the unstable modes, ω, is much larger than the drift frequencies $n\omega_D$ and $k_\parallel v_\parallel$. The passing electrons are assumed adiabatic. As for the RBM, the finite Larmor radius effect are taken in the low wave number limit, where the Bessel functions are taken as $J_o^2(k_\perp \rho_i) \simeq 1 - \frac{k_\perp^2 \rho_i^2}{2}$. The trapped and passing ions and the trapped electrons are taken into account. The lowest order ballooning representation is used. Details of this derivation are given in the appendix D of [40]. In the absence of rotation, and after integrating over energy and pitch angle, one finally

obtains the following dispersion relation:

$$\left[\left(\omega \left(\frac{d_{\text{eff}}^2}{2} d_{xx} - \frac{k_\theta^2 \rho_{\text{eff}}^2}{2} \right) - 2n\bar{\omega}_D + \frac{\dot{k}_\parallel^2 c_{\text{eff}}^2}{2\omega} x^2 \right) \right.$$
$$\left. \times \left(\omega - n\omega_{pi}^* \right) - \frac{f_t}{f_p} n\omega_{pe}^* n\bar{\omega}_d - \omega \left(\omega - n\omega_{ne}^* \right) \right] \bar{\phi} = 0 \tag{7}$$

with $c_{\text{eff}} = \sqrt{T_e/m_p}$, $d_{\text{eff}} = \delta_{\text{eff}}^2 + 4\frac{n\bar{\omega}_d}{\omega}(\hat{s} - \alpha - 0.5)d^2$, $\delta_{\text{eff}} = q^2/(2\epsilon)\rho_{\text{eff}}$, $\rho_{\text{eff}} = \frac{\sqrt{2T_e m_p}}{eB}$, f_t the fraction of trapped particles, $f_p = 1 - f_t$ the fraction of passing particles, $n\omega_{pe}^* = \frac{k_\theta T_e}{eB} \frac{\nabla P_e}{P_e}$ and $n\omega_{ne}^* = \frac{k_\theta T_e}{eB} \frac{\nabla n_e}{n_e}$. Similarly to the RBM derivation, the solution of this second order differential equation is a Gaussian of width $w_{\text{ITG-TEM}}$. Balancing the parallel dynamics with the perpendicular finite width effects gives the expression for $w_{\text{ITG-TEM}}$:

$$w_{\text{ITG-TEM}}^2 = \frac{-\iota \omega d_{\text{eff}}}{\dot{k}_\parallel c_{\text{eff}}} \tag{8}$$

By replacing the values found in equation (8) for $w_{\text{ITG-TEM}}^2$, one then gets a second order polynomial equation for ω such that:

$$\frac{\omega}{2} \left(\omega \left(\omega - n\omega_{ne}^* \right) + \frac{f_t}{f_p} n\omega_{pe}^* n\omega_D \right) \left(\omega + \frac{\tau}{\bar{Z}} n\omega_{pe}^* \right) \tag{9}$$
$$+ \left(2n\omega_D + \frac{\iota \dot{k}_\parallel c_{\text{eff}} d_{\text{eff}}}{2} \right) \left(\omega + \frac{\tau}{\bar{Z}} n\omega_{pe}^* \right)^2 = 0$$

Assuming a dominant curvature such that the interchange term dominates over the others, and assuming further that density profiles are flatter than pressure profiles, one then obtains the following growth rate:

$$\gamma_{\text{ITG-TEM}} = (k_\theta \rho_i)^2 \gamma_I \frac{1}{1 - f_t} \left(f_t + \frac{\tau}{\bar{Z}} \right) \tag{10}$$

So far the impact of collisions on trapped electrons has not been included. It is important to take this effect into account since by scanning the temperature, the collisions are further decreased and, due to weaker detrapping, the TEM get stronger. In the gyrokinetic formulation, the collision frequency is at the denominator with the curvature drift. Therefore it is the ratio between ν and $n\omega_D$ which matters. To reproduce this effect in the fluid approach, a term such as $f_t \frac{\nu}{n\omega_D}$ is added. Since higher collisionality leads to weaker TEM, hence weaker growth rate, one obtains:

$$\gamma_{\text{ITG-TEM}} =$$
$$(k_\theta \rho_i)^2 \gamma_I \frac{1}{1 - f_t} \sqrt{\left(f_t + \frac{\tau}{\bar{Z}} \right)^2 - \left(0.07 f_t \frac{\nu}{n\bar{\omega}_{de}} \right)^2}$$

The factor 0.07 has been adjusted to match a temperature scan done with Gene as illustrated by figures 1 and 2. In the case of $\left(f_t + \frac{\tau}{\bar{Z}} \right)^2 < \left(0.07 f_t \frac{\nu}{n\bar{\omega}_{de}} \right)$, ITG only are assumed to be unstable and in this case:

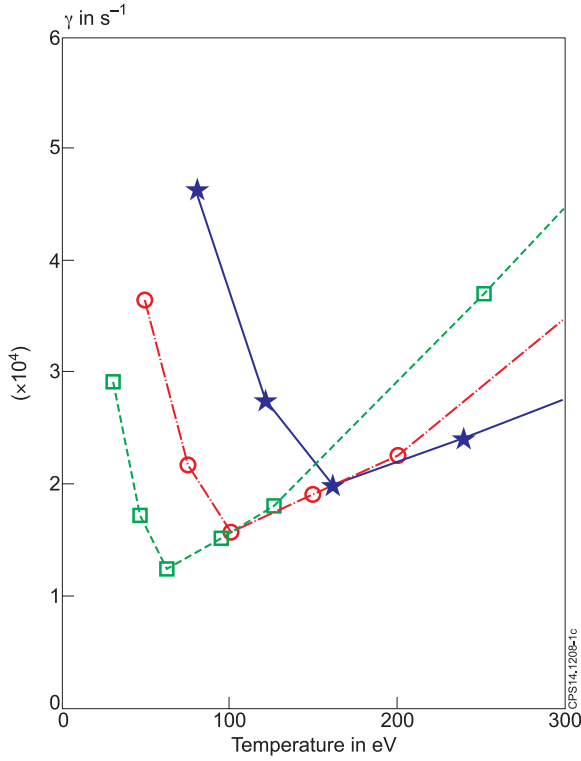$$\gamma_{\text{ITG}} = 0.2(k_\theta \rho_i)^2 \gamma_I \frac{1}{1 - f_t} \frac{\tau}{\bar{Z}} \tag{11}$$

Figure 1. Growth rate computed by Gene at $k_\theta \rho_i = 0.1$ of the most unstable mode versus the temperature for the parameters as given in table 1, except changing n from 2.6×10^{19} m^{-3} down to 1×10^{19} m^{-3} and 0.4×10^{19} m^{-3}.

Figure 2. Growth rate in the analytical fluid limit versus the temperature for the parameters as given in table 1, except changing n from 2.6×10^{19} m^{-3} down to 1×10^{19} m^{-3} and 0.4×10^{19} m^{-3}.

2.2.3. Comparison of the analytical turbulence growth with a Gene *linear simulation.* A growth rate for the RBM branch and one for the ITG-TEM branch have been derived analytically. They are derived for a fixed value of $k_\theta \rho_i$, this means that the wave length is assumed to scale with ρ_i and that this fixed $k_\theta \rho_i$ is representative of the whole spectrum of modes.

The way RBM and ITG-TEM branches compete over a temperature scan is studied for a set of parameters inspired by a JET-ILW pulse prior to the transition into H mode, taken as in [14]:

The density, 2.6×10^{19} m^{-3} at $\rho = 0.97$, is changed to two other lower values: 0.4×10^{19} m^{-3} and 1×10^{19} m^{-3}. If the density is decreased, the collisionality decreases leading to weaker RBM and stronger TEM contribution to the ITG-TEM branch [41]. This is what is reported in figure 1 for Gene and on figure 2 for the analytical model detailed above.

The value of $k_\theta \rho_i$ is chosen arbitrarily within the range over which RBM, destabilized by larger collisionality, are reported, i.e. $k_\theta \rho_i < 0.4$. In the following $k_\theta \rho_i = 0.1$ is chosen. Note that for $k_\theta \rho_i = 0.3$ the minimum of the growth rate is shifted towards larger temperatures. Therefore the present work limits itself to qualitative insights pointing towards the potential role of RBM. Clearly, non-linear effects could give more important weight to different wave-numbers, and should be addressed by future works.

In the fluid limit, the growth rate is the maximum of the RBM and the ITG-TEM growth rate, such that: $\gamma_{\mathrm{turb}} = \max(\gamma_{\mathrm{RBM}}, \gamma_{\mathrm{ITG-TEM}})$. On figure 2 both RBM and ITG-TEM branches are displayed for three values of density as a function of temperature. As expected, the RBM growth rates decrease
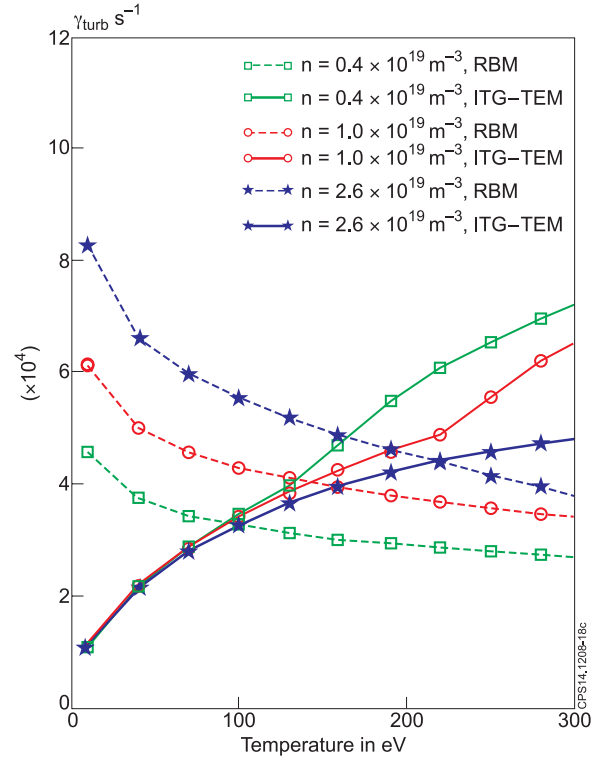
as the temperature increases, whereas the ITG-TEM growth rate increases with larger temperatures. The maximum of both branches reaches a minimum value at a given temperature. Note that the stabilization by the MHD parameter α occurs at temperatures at least 4 times larger than the experimental range as illustrated in appendix A.

Although not exact, one can see that the fluid model leads to a minimum growth rate at a temperature similar to the Gene calculation: 150–200 eV for $n = 2.6 \times 10^{19}$ m^{-3} and rather 50–100 eV for n from $n = \times 10^{19}$ m^{-3}. On the ITG-TEM branch, as the density is increased, the collisionality is larger and the TEM are weaker leading to weaker growth rates. This is seen on the Gene modeling and also in the analytical ITG-TEM branch. On the analytical model, this trend was obtained by setting a free parameter to 0.07 in front of the collision part of equation (11). The analytical growth rates are larger than the computed ones with Gene. Indeed, the fluid limit is known to overestimate the growth rates when compared to a gyrokinetic calculation.

In the following, the analytical growth rates will be calculated at fixed $k_\theta \rho_i$. The choice for $k_\theta \rho_i$ is arbitrary. Nonetheless, from non-linear simulations of ITG-TEM, it is known that non-linearly there is a down-shift of the highest turbulent activity towards lower $k_\theta \rho_i$. In the following $k_\theta \rho_i = 0.1$ is chosen.

3. The mean E_r shearing time: $1/\gamma_E$

An analytical formulation of the turbulence growth rate, γ_{turb}, has been derived. In the following the derivation of the time scale of the competing mean E_r shear, γ_E, is presented.

Table 1. Edge parameters for a JET-ILW discharge 82228 prior to the L to H transition.

Pulse	ρ	R/L_T	R/L_n	T	n	ν^*	q	s	Z_{eff}	B
82228	0.97	55	9	122	2.6	9.2	3.8	4.3	1.3	1.8

Note: The temperature is given in eV, the density n in $10^{19}\,\text{m}^{-3}$ and the magnetic field B in T.

3.1. Experimental justification for the E_r shearing

Thanks to recent progress made on E_r measurements, either directly by Doppler reflectometry as in [17] or indirectly by simultaneous poloidal and toroidal rotation measurements using edge charge exchange spectroscopy as in [42–44], the experimental detailed dynamics and values of E_r at the transition are better known. Recent experimental measurements in ASDEX Upgrade strongly support the essential role of the ion channel in the L-H transition, via the diamagnetic E_r provided by the ion pressure gradient [16, 45]. These results indicate that the E_r well has to reach a certain depth amplitude to permit the transition into H-mode. In JET-ILW, recent analysis of the back transition from H to L mode [15] show that similar inferred diamagnetic E_r are found at the forward and back transitions. These two recent experimental observations support the theory of a critical mean E_r shear suppressing turbulence at the L-H transition as proposed long ago [7]. On the other hand, the dynamics of the transition (measured by Doppler reflectometry, heavy ion beam probes, Langmuir probes and/or Beam Emission Spectroscopy) is reported to consist of oscillatory features [17–19]. These oscillatory behaviors might be providing evidence that low frequency, turbulence-generated Zonal Flows are key to trigger turbulence suppression preceding the L-H transition, although this interpretation is discussed in [19] and [46]. In all cases, the final word seems to be given by the mean E_r shear to lock down the turbulence level. In the following, the mean E_r shear is derived. The idea here, is to remain as simple as possible, while not forgetting essential mechanisms. If the parametric dependencies of the ratio of $\gamma_{\text{turb}}/\gamma_E$ are coherent with the main threshold dependencies, then further improvements of the shearing rate modeling could be foreseen, for example, to account for the turbulence driven ZF.

3.2. The modeled γ_E

To estimate the mean E_r shear, the electric field is estimated at two radial locations. One is the last closed flux surface, where E_r is known to scale with ∇T_e [47] and was found experimentally in JET to be $E_r(1) = -1.6\nabla T_e$ and in ASDEX-Upgrade, TCV and JT60-U rather $E_r(1) = -3\nabla T_e$. This latter formula has been shown to agree with an analytical model for the electrostatic potential in [48] in the sheath limited case for Hydrogen. Ideally, as suggested in [48], the combined effect of both the sheath and the main SOL plasma dynamics should be taken into account to estimate E_r at the LCFS. For the time being, only its dependence on T_e is included here by fixing $E_r(1) = -3\nabla T_e$. If assuming a temperature profile having a fixed gradient length in the pedestal forming region and across the separatrix, one gets:

$$E_r(1) = 3\frac{T_{\text{sep}}}{L_T} \tag{12}$$

L_T is the temperature gradient length and is kept constant to its value at $\rho = 0.97$ even at the LCFS. Assuming an exponential fit of the temperature in this region, one obtains:

$$T_{\text{sep}} = T(0.97)e^{(-0.03a/L_T)} \tag{13}$$

For the values of table 1, this leads to $T_{\text{sep}} = 70\,\text{eV}$ and $E_r(1) = 3.9\,\text{kV}\,\text{m}^{-1}$.

The other E_r value is chosen at a radial location which is kept fixed. This means that the shear is modified by the two radial location values and not by a modified inner localization of the minimum of E_r. In H mode, this has been studied [43] and the E_r well position was shown to depend only on a. This point remains to be experimentally investigated in L mode prior to the transition. For the time being, in the approach presented here, the inner location is arbitrarily chosen to be $\rho = 0.97$ and is assumed to remain fixed through the various parametric scans. At this inner location, E_r is estimated as follows:

$$E_r = \frac{\nabla P}{Z_i n} - V_\theta B_\varphi + V_\varphi B_\theta \tag{14}$$

In the following, the toroidal velocity, V_φ, term is neglected. Indeed, in JET-ILW, with low NBI, edge charge exchange measurements have found that V_φ was lower than the uncertainties of the measurements for low NBI levels prior to the transition in the pedestal forming region [49]. In ASDEX Upgrade, in [42], also with edge charge exchange measurements, the toroidal velocity profile is found to be finite but flat in the pedestal forming region in L mode. Its contribution to E_r is weaker than the V_θ term.

For the determination of the poloidal velocity, V_θ, the neoclassical theory is used. In the edge region, ν^* varies strongly from below 1 to above 1, therefore it is essential to model properly the transition from the banana, plateau and Pfirsch–Schlutter regimes. This is done using the analytical formulation proposed in [50], such that:

$$V_\theta = K_{\text{neo}} \frac{1}{B_\varphi Z_i} \nabla T_i \tag{15}$$

with Z_i the charge number of the main ions, $K_{\text{neo}} = \frac{K_{bp} - 2.1\nu_i^{*2}\epsilon^3}{1 + \nu_i^{*2}\epsilon^3}$ and $K_{bp} = \frac{1.17 - 0.35\sqrt{\nu_i^*}}{1 - 0.7\sqrt{\nu_i^*}}$, $\nu_i^* = \frac{\nu_i}{\epsilon^{3/2}\frac{V_{thi}}{qR}}$, $\nu_i = \nu_e \sqrt{m_e/m_i}$ and $\nu_e = \nu$ defined earlier. This formulation is an extrapolation among different analytical limits. This extrapolation could be carried out diversely as reported in [51]. In [44], the analytical formulation from [50] has been successfully compared to numerical neoclassical modeling as well as to the measured V_θ in H mode plasmas only. Nonetheless it is puzzling to note that the neoclassical and measured E_r at the LCFS lead to negative values in disagreement with SOL physics expectations. More work is needed in this field, both theoretically and experimentally. Experiments
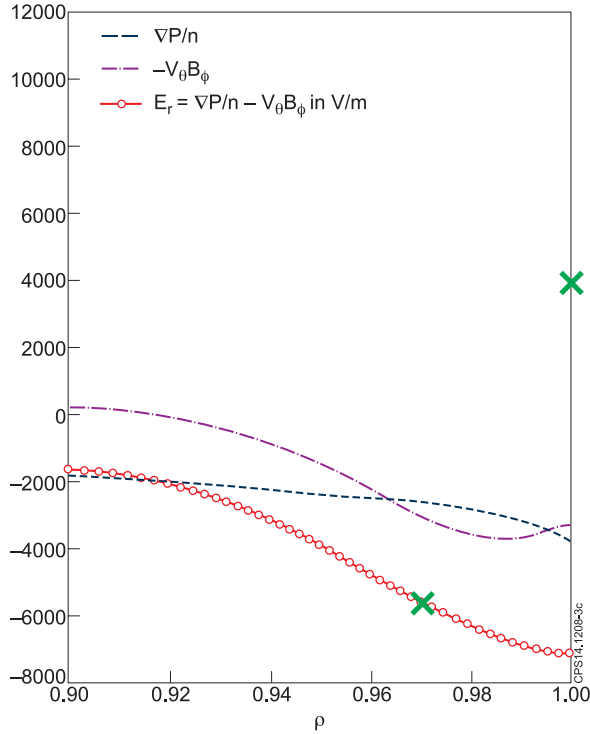
Figure 3. In blue the E_r contribution due to the pressure gradient, in purple the contribution due to V_θ and in red the sum of both. In green are represented the two values used for the γ_E estimate, at $\rho = 0.97$ and at the LCFS. The profiles used for these estimates are based on the JET-ILW pulse 82228 prior to the transition in H mode reported also in table 1.

with simultaneous SOL measurements with probes and charge exchange and/or Doppler reflectometry measurements in the edge should shed light on how and where the core neoclassical constrain and the SOL constrain on E_r merge in one unique profile. Advances in codes able to simultaneously model the core and the SOL such as [52, 53] will also help clarifying this point. In the present work, two values of E_r are chosen: a first one at $\rho = 0.97$ following the neoclassical theory predictions and second one at the LCFS following the SOL physics expectation. Despite the fact that the precise radial locations of these two limits is disputable, it is assumed that they give appropriate qualitative trends for the shear derivation in the edge region.

From the two E_r values, at the LCFS and at $\rho = 0.97$, a shearing rate is derived such that:

$$\gamma_E = \frac{\nabla E_r}{B} = \frac{E_r(0.97) - E_r(1)}{0.03 \times a \times B} \qquad (16)$$

The derivative of E_r is taken with respect to the flux surface coordinate which is the square root of the toroidal flux. On figure 3, in purple, the two values used to estimate the E_r shear are illustrated for the parameters from table 1. The radial variation of E_r is mostly impacted by the V_θ term which varies due to ν^* variations in this edge region. The LCFS value of E_r is positive as expected.

Here the role of a potential residual stress modifying the poloidal velocity is not taken into account, whereas it could be an important player in some cases. Indeed, experimentally it has been observed by Beam Emission Spectroscopy [54] that

the poloidal velocity in the edge region is modified in case of grad-B drift direction reversal. In [55], an explanation is proposed through a modified residual stress in case of grad-B drift reversal. Such effects could be added to the present model in a later stage. Detailed L mode V_θ investigation and comparison to models prior to the transition are required.

For the time being, γ_E depends on the temperature but also on n, L_n, L_T, Z_{eff}, a, R, q, B and Z_i.

4. Parametric dependencies of the ratio between the mean field time scale and the turbulence time scale: γ_{turb}/γ_E

In the two previous sections, two times, one characterizing the turbulence and the other the mean E_r shear, have been analytically derived. A lowered ratio of γ_{turb}/γ_E is taken as an indication for a facilitated entry into H mode. Therefore, since the H mode power threshold is known to scale with B, the density, Z_{eff}, etc, such dependencies should be qualitatively recovered through the dependencies of γ_{turb}/γ_E. This is what is investigated in this section.

4.1. Magnetic field impact

The power threshold increases almost linearly with B [2, 3], either with q changing or with q fixed as demonstrated in JET-ILW in [15]. Therefore, it seems to be B per se which matters. On the turbulence side, B, at fixed q, could play a role through β but the turbulence in the studied L mode edge at low β is expected to be electrostatic due to the ordering of terms of the Ohm's law as detailed in appendix B. At fixed $k_\theta \rho_i$, larger q leads to more unstable RBM. This trend is qualitatively coherent with TCV L mode experiments where the electron temperature gradient lengths are found to increase with I_p in the edge region [12]. At fixed q, in the electrostatic case, B impacts weakly γ_{turb} through modified α. As T increases, γ_{turb} goes from RBM to ITG-TEM dominated regime as illustrated by the top panel of figure 4. On the contrary, γ_E increases with T and is weaker for larger B as seen on the middle panel of figure 4. Therefore a given value of γ_{turb}/γ_E is reached for larger T as B increases, see bottom panel of figure 4. If the temperature threshold is defined as the temperature above which γ_{turb}/γ_E is smaller than a given value, then one finds that T_{th} increases with larger B for any critical value of γ_{turb}/γ_E as illustrated by figure 5.

The dependence of γ_{turb}/γ_E with respect to B leads to $T_{th} \propto B^{\alpha_B}$ with a positive value of α_B for any critical value of γ_{turb}/γ_E. Indeed for $\gamma_{turb}/\gamma_E = 0.3$, respectively 0.15, one finds $\alpha_B = 1.0$, respectively 1.5, as illustrated by figure 5. This trend is in agreement with all the experimental reported behaviors of the temperature threshold reviewed in the introduction. More interestingly, it explains the robust, almost linear, scaling of the power threshold P_{th} with $n \times B \times S$ [1–3]. Due to the γ_E dependence on $1/B$ from equation (16), one obtains $T_{th} \propto B$ and hence at least $P_{th} \propto nBS$.

4.2. Density impact

A common and robust trend of all machines and scaling laws is an increase of the power threshold with higher density above
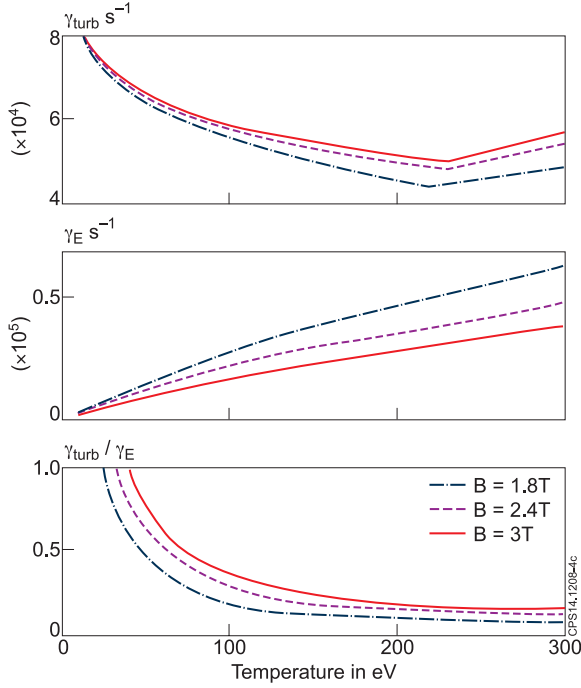
Figure 4. Top panel: turbulent growth rate γ_{turb} in s^{-1} as a function of temperature in eV for three values of the magnetic field at fixed q. Note that the RBM branch is dominant at low temperature where the growth rate decreases with increasing temperature and the ITG-TEM dominate at larger temperature with increasing growth rates for higher temperatures. Middle panel: mean flow shearing rate γ_E in s^{-1} as a function of temperature in eV for same three magnetic field values. Bottom panel, the ratio of γ_{turb}/γ_E as a function of temperature for the same three values of B.
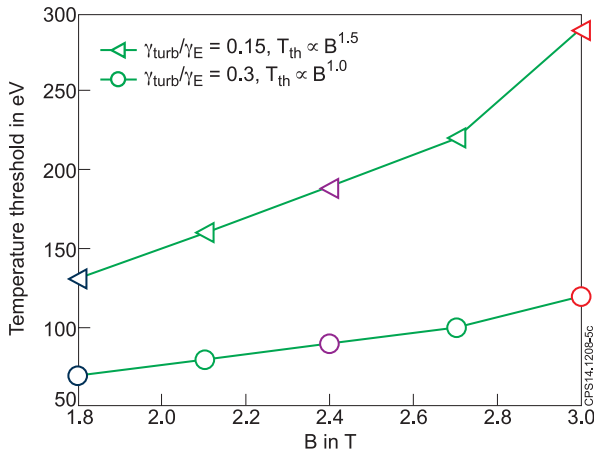

Figure 5. Temperature threshold versus magnetic field, at q fixed, for two values of γ_{turb}/γ_E. For $B = 1.8$ T, 2.4 T and 3 T, the values are respectively signaled by the same colors used for figure 4, the other parameters are as reported in table 1.

a certain density. At low density, a roll-over of the dependence on density is reported in most machines [1]. In JET with the MkII-HD geometry and the C wall, the power threshold was not seen to roll-over at low density, whereas in JET-ILW it was [15].

Above the density roll-over, the dependence of the temperature threshold with density is weaker [4] than the dependence of P_{th} which is close to linear [1–3]. A weaker trend for T_{th} might be expected since $P_{th} \propto SnT_{th}\chi_{eff}/L_T$.

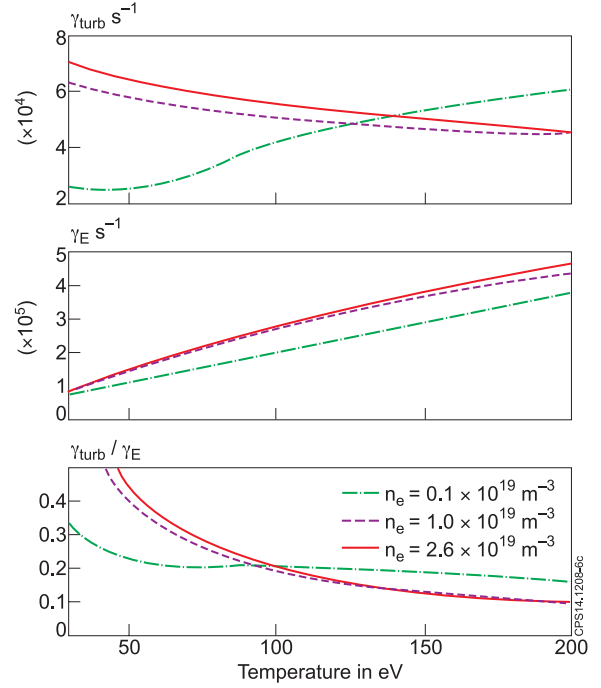**Figure 6.** Top panel: γ_{turb} in s^{-1} as a function of temperature in eV for three values of n. Middle panel: mean flow shearing rate γ_E in s^{-1} as a function of temperature in eV for three densities. Bottom panel, the ratio of γ_{turb}/γ_E as a function of temperature for the same three n values.

The very weak dependence of the temperature at the threshold with density, on the high density branch, is also reported in recent JET-ILW, AUG and Alcator C-Mod works [15, 16, 27]. In these works, on the contrary, the low density branch is associated with a clear increase of electron temperatures as the density is reduced. The behavior of T_{th} versus density below and above the roll-over density will be recovered.

In the modeled turbulence growth presented here, increasing the density leads to larger collisionality, hence more unstable RBM. The $E \times B$ shearing is not affected by a modified density for the lower temperatures. For larger temperatures, the ITG-TEM branch takes over and is stabilized by larger densities. On the other hand, γ_E is increased by larger densities. The temperature impact on γ_{turb} and γ_E for three densities are illustrated by figure 6.

As a consequence, two opposite trends are observed at low temperatures (below 50–100 eV) and at high temperatures (above 50–100 eV). At low temperatures, a higher density leads to lower T_{th}, whereas above 50–100 eV, a higher density leads to a weakly increasing T_{th}, as observed for the ratio of $\gamma_{turb}/\gamma_E = 0.15$ illustrated on figure 7. Nonetheless this trend is sensitive to the arbitrary choice of the critical value of γ_{turb}/γ_E below which one enters in H mode. Indeed, for $\gamma_{turb}/\gamma_E = 0.3$ and the set of parameters from table 1, only a weak increase of T_{th} versus density is reported, figure 7.

4.3. Impact of the effective charge

The effective charge was reported as an important ingredient of the scaling law in [2], other experimental facts pointing towards the potential impact of Z_{eff} on the power threshold are reported in [14]. Recently, in JET-ILW, the ITPA 2004 scaling
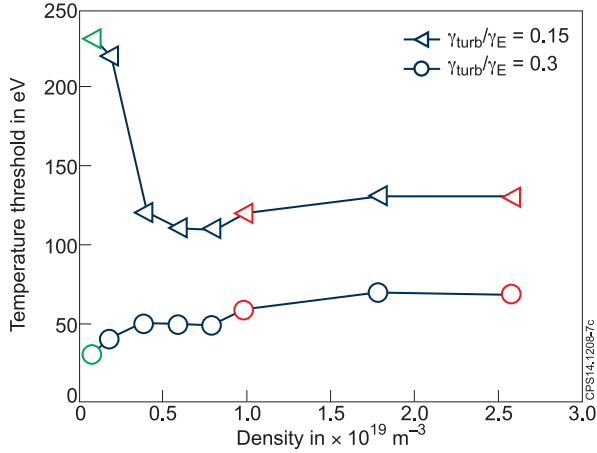
Figure 7. Temperature threshold versus density, for two values of $\gamma_{\text{turb}}/\gamma_E$, the other parameters are as reported in table 1.

Figure 8. Temperature threshold versus density, for $Z_{\text{eff}} = 1.3$ and a mix of D and Be and for $Z_{\text{eff}} = 2.2$ and a mix of D and C, the other parameters are as reported in table 1 and $\gamma_{\text{turb}}/\gamma_E = 0.15$.

Figure 9. Temperature threshold versus density, for $T_i/T_e = 1$ and for $T_e = 50$ and $100\,\text{eV}$, the other parameters are as reported in table 1 and $\gamma_{\text{turb}}/\gamma_E = 0.15$.

law including a Z_{eff} dependence has been shown to reconcile better JET-C and JET-ILW observations [33].

Z_{eff} has opposite impacts at low temperatures where RBM are dominant and at higher temperatures where ITG-TEM dominate. Indeed, a higher Z_{eff} destabilizes the RBM branch, due to larger collisionality and stabilizes the ITG-TEM due to dilution and collisionality impacts. Concerning the $E \times B$ shear, modifying Z_{eff} impacts V_θ contribution to E_r through a modified collisionality. The dilution also affects the pressure gradient term in E_r. γ_E dependence on Z_{eff} could not explain the observed trend of a larger power threshold for larger Z_{eff} discused earlier. Indeed, γ_E, if anything, is larger for larger Z_{eff}. Overall, at low temperatures, a lower temperature threshold due to lower Z_{eff} is due to reduced RBM growth.

For $\gamma_{\text{turb}}/\gamma_E = 0.15$ and for two values of Z_{eff}, 2.2 and 1.3, respectively in the range found in JET-C and JET-ILW, the temperature threshold versus density exhibits a shift of its minimum towards lower values for the higher Z_{eff}, see figure 8. This shift downward is explained by more stable ITG-TEM and more unstable RBM. Such a shift is consistent with the fact that in JET-ILW the minimum in density has reappeared whereas in the same divertor configuration (MkII-HD) but with the C wall this minimum was not in the range that could be measured experimentally. Nonetheless, it is to note that on the high density branch, the experimentally stabilizing impact of Z_{eff} is not reproduced here.

4.4. Impact of T_i/T_e

As discussed previously, experimentally, the low density branch is associated with a larger electron temperature [15, 16, 27]. In ASDEX Upgrade, with ECRH only, it is also reported that the low density branch is associated with a strong decoupling between ion and electron heat channels with $T_e > T_i$. In these cases, the edge ion heat flux, $q_{i,\text{edge}}$, at the L-H transition increases monotonically with the density (rather than non-monotonically as $P_{\text{L}-\text{H}}$) indicating that $q_{i,\text{edge}}$ could be the relevant parameter [16, 45]. In JET-ILW, where $T_e = T_i$ even on the low density branch, a non-monotonical density trend remains with a minimum in density. On ASDEX Upgrade, $T_e > T_i$ is systematically associated with the low density
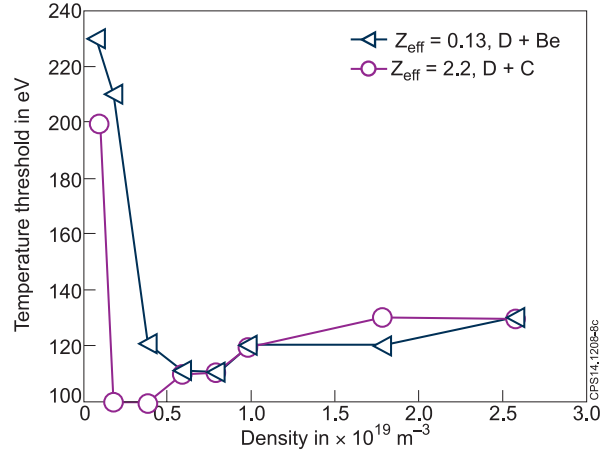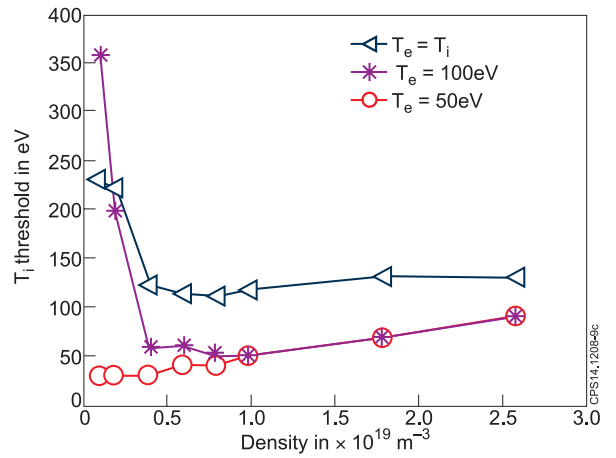
branch, whereas in JET $T_e = T_i$ also below the minimum in density.

In the following, the T_{th} sensitivity to T_e/T_i is investigated. In particular, the T_{th} dependence versus density at $T_i = T_e$ plotted on figure 7 is compared to the case where T_e is kept fixed at 50 and 100 eV while T_i is scanned. The comparison is made for $\gamma_{\text{turb}}/\gamma_E = 0.15$ and is illustrated on figure 9.

From figure 9, it can be seen that the dependence of T_{th} on density is strongly modified by the value of T_i/T_e. In particular the minimum in density disappears when T_e remains fixed at 50 eV while T_i is scanned. Indeed, the impact of T_i/T_e is expected on both the turbulence drive and on the $E \times B$ shear.

First, concerning the turbulence drive, as T_i/T_e increases, the RBM drive is stronger, see the τ dependence in equation (5). This trend is illustrated by figure 10 where the growth rates are plotted versus T_i at either fixed $T_e = 100\,\text{eV}$ or such that $T_i = T_e$, for two density values. For the $T_e = 100\,\text{eV}$ cases, in full lines, when T_i is such that $T_i > 30\,\text{eV}$, it can be seen that a larger density is destabilizing due to the RBM nature of the modes for larger T_i/T_e. This trend is reversed for low T_i values where the ITG-TEM branch dominates.
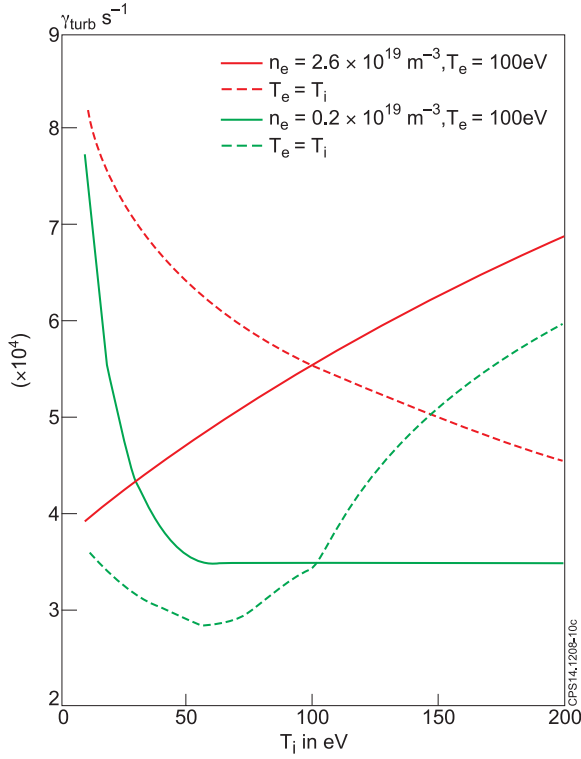
Figure 10. Turbulent growth rate γ_{turb} in s^{-1} as a function of T_i in eV, T_e being fixed at 100 eV full lines and for $T_e = T_i$ dashed lines, for two density values: 2.6×10^{19} m^{-3} in red and 0.2×10^{19} m^{-3} in green.

Figure 11. $E \times B$ shearing rate γ_E in s^{-1} as a function of T_i in eV, T_e being fixed at 100 eV full lines and for $T_e = T_i$ dashed lines, for two density values: 2.6×10^{19} m^{-3} in red and 0.2×10^{19} m^{-3} in green.

The second reason is that E_r at the LCFS depends on T_e, while E_r at $\rho = 0.97$ depends on T_i. Indeed E_r at $\rho = 0.97$ or, the E_r well mentioned in [45], scales with T_i. If the E_r shear is determined by the gradient between the well and the LCFS, as assumed here, the T_i/T_e ratio will impact γ_E. Indeed, for $T_i > T_e = 100$ eV (full lines), γ_E is smaller than its value obtained for $T_i = T_e$ (dashed lines), as illustrated by figure 11.

Therefore when $T_e > T_i$, the RBM drive is weaker and due to larger $E_r(1)$, γ_E is larger, leading to lower T_{th} as reported on figure 9. For $T_e = 50$ eV, the RBM are dominant at all densities and in this case the minimum, due to a switch from underlying ITG-TEM to RBM, disappears. This trend is coherent with the results reported from ASDEX-Upgrade [16, 45].

4.5. Isotopic effect

A higher power threshold in H compared to D has been reported in various machines. The scaling with the mass number is significant: $P_{\text{th}} \propto A_i^{-1}$, as reported in [1, 21]. It was also reported that the temperature threshold itself depended on A_i such that $T_{\text{th}} \propto A_{\text{eff}}^{-0.14 \pm 0.19}$ [20]. At fixed $k_\theta \rho_i$, as it has been chosen here, the interchange growth rate scales as $1/\sqrt{A_i}$. A_i has no impact on the $E \times B$ shearing rate in the case where the potential at the LCFS is set by adiabaticity [48]. If the potential is set by the sheath, then larger A_i will lead to higher E_r at the LCFS [56], hence greater $E \times B$ shear. Therefore, in all cases, larger A_i leads to lower $\gamma_{\text{turb}}/\gamma_E$. The temperature threshold obtained for $\gamma_{\text{turb}}/\gamma_E = 0.15$ when changing the main ion from D to H is largely increased assuming fixed Z_{eff}, q, T_i/T_e, gradient lengths, etc., as illustrated on figure 12.
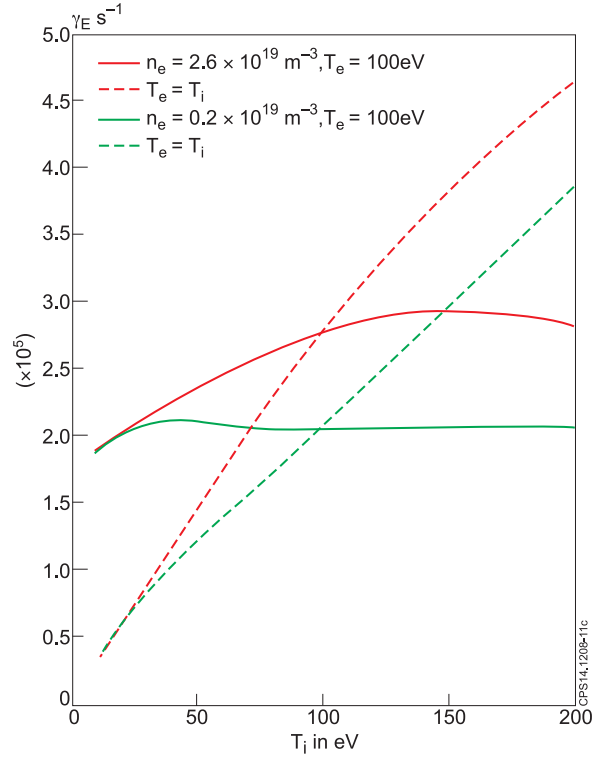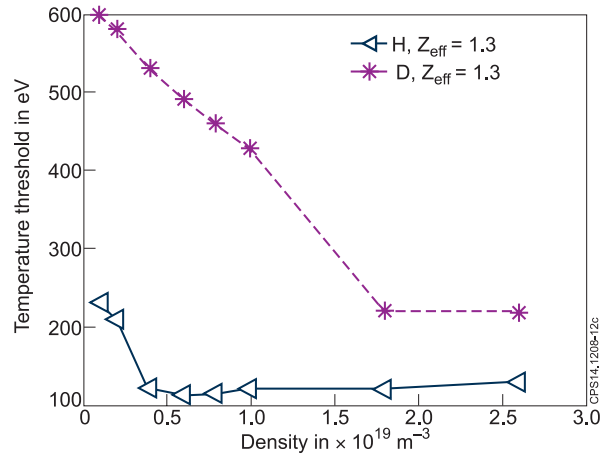

Figure 12. Temperature threshold versus density, for D and H, the other parameters are as reported in table 1 and $\gamma_{\text{turb}}/\gamma_E = 0.15$.

4.6. Helium versus deuterium effect

A recent multi-machine effort has been carried out to study the power threshold in He and compare it to the one obtained in D. These efforts are summarized in [57]. A higher power threshold with He is seen in Alcator C-Mod and DIII-D, whereas no impact is reported in JET [58] and ASDEX-Upgrade. In the modeling proposed here, by changing both the mass and the charge and keeping A_i/Z_i constant, nothing is modified on the turbulence drive. The neoclassical E_r is modified by a modified Z_i. Indeed $V_\theta \propto 1/Z_i$, hence a higher Z_i leads to a lower absolute value of $E_r(0.97)$ and therefore a weaker γ_E. A_i modifies the LCFS value if the potential is
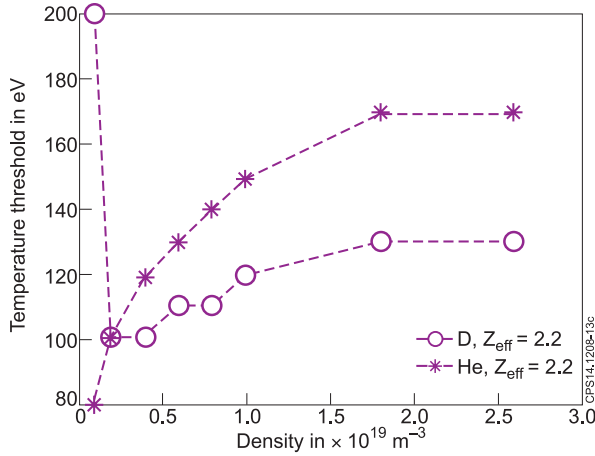
Figure 13. Temperature threshold versus density, for D and He, the other parameters are as reported in table 1 and $\gamma_{\mathrm{turb}}/\gamma_E = 0.15$.

set by the sheath [48, 56], otherwise it does not impact E_r. If the potential is set by the sheath, then the $E \times B$ shearing rate is impacted by two contradictory trends: one due to higher Z_i leading to weaker shear, and one due to higher A_i leading to larger E_r at the LCFS. Two cases are looked at: one with $E_r(1)$ independent of A_i and one where A_i modified $E_r(1)$. Here Z_{eff} has been assumed to be independent of the change from D to He and was kept constant at $Z_{\mathrm{eff}} = 2.2$. This is an assumption made here to test the impact of the ion species in the proposed model. The experimental impact on Z_{eff} when changing the main ions from D to He should be investigated further. If $E_r(1)$ does not depend on A_i, changing from D to He leads to a higher $\gamma_{\mathrm{turb}}/\gamma_E$, leading to lower T_{th} in D than in He as illustrated by figure 13. This is consistent with power thresholds higher in He than in D. If the potential is set by the sheath, then the $E \times B$ shearing rate is impacted by two contradictory trends: one due to a higher Z_i leading to a weaker shear, and one due to a higher A_i leading to a larger E_r at the LCFS. Under these conditions, almost no impact of changing D to He on T_{th} is observed.

Therefore, depending on the cases, where the potential at the LCFS is set by adiabaticity or by the sheath, one expects respectively that the temperature threshold in He will be larger than in D or similar. This physical mechanism could explain the variety of results reported in [57], where the power threshold in He is either larger of unaffected when compared to D. One should also note that here Z_{eff} has been kept fixed while comparing D to He. Experimentally, that might not be the case. A larger Z_{eff} together with He compared to a lower Z_{eff} and D, would also annihilate the stabilizing effect of He observed on figure 13.

5. Discussion

The approach proposed here is based on robust physical ideas: the turbulence and $E \times B$ interplay on the one hand and the stabilization of RBM on the other hand. The turbulence and the $E \times B$ shear are characterized by two time scales, resp. γ_{turb} and γ_E, which are compared to each other through the ratio $\gamma_{\mathrm{turb}}/\gamma_E$. The growth rate of the turbulent contribution derived analytically, for both RBM and ITG-TEM, is shown

to reproduce closely the main trends of a complete linear gyrokinetic simulation. In particular, when scanning up the temperature, a minimum in the growth rate is obtained as a result of the competing RBM with ITG-TEM for temperature values within the experimental range of the transition into H mode. The mean E_r shear estimation is based on two values: the E_r value at an inner location which accounts for the fact that the collisionality regime is changing rapidly in this region; E_r at the LCFS which is constrained by SOL physics and scales with ∇T_e [48, 56]. This approach can then robustly produce a temperature threshold T_{th} as experimentally reported in [4–6, 11, 15, 20, 27] and explain various parametric dependencies such as:

- a T_{th} increase with B
- larger T_{th} for densities below the minimum in density while being weakly affected above the minimum
- an upward shift of the minimum in density with reduced Z_{eff}
- a T_{th} reduced for lower T_i/T_e, in particular the sensitivity of the low density branch to the value of T_i/T_e
- a higher T_{th} in H than in D
- at fixed Z_{eff} and $E_r(1)$ a higher T_{th} in He than in D.

Nonetheless, the main approximations of this approach are subject to discussion:

- The turbulence is assumed to scale with the main ion Larmor radius. The value of $k_\theta \rho_i$ remains fixed to 0.1. Non-linear modeling has to be carried out to include potential scale modification impacts.
- The E_r shear is assumed to scale with the minor radius, which has recently been shown to be correct in H mode [43] but has not been studied prior to the transition.
- The density and the temperature profiles are assumed to have unchanged gradient lengths across the pedestal forming region.
- The toroidal rotation contribution in E_r is neglected, whereas it is proposed to be a key element in [46].
- The role of a residual stress generating additional perpendicular rotation on E_r is not taken into account here, whereas it is proposed to be linked to the grad-B drift direction impact on the threshold in [55].
- The neoclassical estimate of E_r in the edge region leads to a negative E_r at the LCFS which is inconsistent with the SOL constrain on a positive E_r. Deeper experimental and theoretical understanding of the edge-SOL E_r are required.
- Dithering L-H transitions are observed [17–19] and proposed by some authors to be explained by an interplay with the zonal and the mean flows [17, 18]. Such dynamical non-linear interplay is not addressed by the present approach.
- Finally, only a local variable such as T_{th} can be derived from this approach. Going from the derived T_{th} trends to P_{th} parametric dependencies is not straightforward.

Nevertheless, it is interesting to note that the ingredients of the model (namely: RBM and E_r using $V_\theta(\nu^*)$) are included in a flux driven fluid non-linear modeling which has recently demonstrated its ability to obtain an edge transport barrier when the power is increased [59, 60]. These flux driven fluid simulations should now include Drift Waves and ITG-TEM as well and study the parametric dependencies of the power threshold.
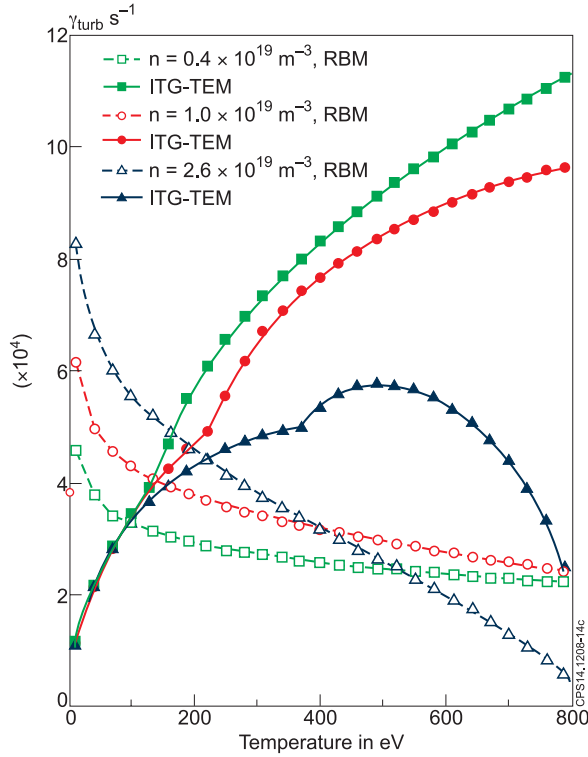
Figure 14. RBM and ITG-TEM growth rates in the fluid limit versus the temperature for the parameters of table 1, except changing n from 2.6×10^{19} m^{-3} down to 1×10^{19} m^{-3} and 0.4×10^{19} m^{-3}.

Figure 15. Ratio $\frac{\gamma_{\text{RBM}}}{\frac{\eta}{\mu_0} k_\perp^2}$ versus temperature in eV, for two values of density, the other parameters are as reported in table 1.

Appendix B. Validity of the electrostatic approximation

Following the discussion presented in section 2.2, the RBM are estimated analytically in the electrostatic limit. This assumption is justified a posteriori by comparing the terms of the Ohm's law:

$$\eta J_\parallel = -\mathrm{i}\left(\omega A_\parallel - k_\parallel \phi\right)$$

Using the Ampere's law:

$$\nabla_\perp^2 A_\parallel = -\mu_0 J_\parallel$$

One finds that the electrostatic limit is adequate if $\gamma A_\parallel \ll \eta J_\parallel$, hence if $\gamma \ll \frac{\eta}{\mu_0} k_\perp^2$.

In section 2.2, γ_{RBM} and w_{RBM} have been derived. Since $k_\perp^2 = \left(\frac{2\pi}{w_{\text{RBM}}}\right)^2 + k_\theta^2$ and $\gamma = \gamma_{\text{RBM}}$, one can check the validity of the electrostatic approximation using the edge JET-ILW parameters presented in table 1. Such a check is illustrated by figure 15 where it is found that γ_{RBM} is a least two orders of magnitude lower than $\frac{\eta}{\mu_0} k_\perp^2$ which justifies the electrostatic limit used for the analytical derivation.

Also when using the linear gyrokinetic code Gene on the various sets of L mode edge parameters [13, 14] it was observed that including magnetic fluctuations did not affect the linear response.

Appendix A. Stabilization by α

The fluid limit analytical formulations for the RBM and ITG-TEM growth rates (respectively equations (5) and (11)) are plotted versus temperature as illustrated by figure 2. Here the temperature range is extended up to $T = 800$ eV. On figure 14, the stabilization impact due to large α takes over the destabilizing reduced collisionality for temperatures above 500 eV. For larger densities, due to larger α, the stabilization occurs at lower temperatures. Similarly higher q favors the α stabilization.
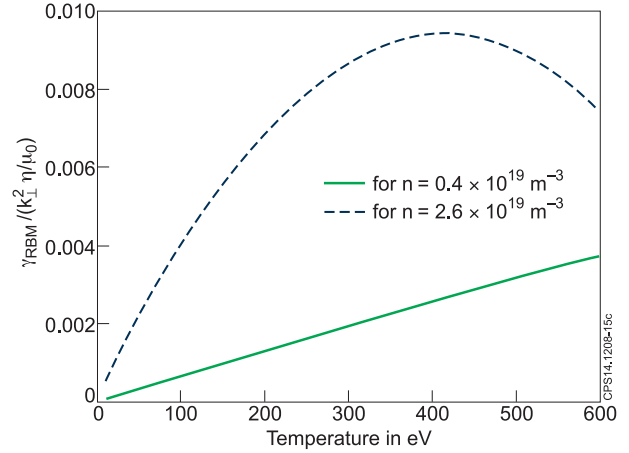
References

[1] Ryter F. *et al* 1996 H mode power threshold database for iter *Nucl. Fusion* **36** 1217

[2] Takizuka T. and ITPA H-Mode Database Working Grp 2004 Roles of aspect ratio, absolute B and effective Z of the H-mode power threshold in tokamaks of the ITPA database *Plasma Phys. Control. Fusion* **46** A227–33

[3] Martin Y.R., Takizuka T. and the ITPA CDBM H-mode Threshold Database Working Group 2008 *J. Phys.: Conf. Ser.* **123** 012033

[4] Meakins A.J., McDonald D.C. and EFDA-JET contributors 2010 The application of classification methods in a data driven investigation of the jet l-h transition *Plasma Phys. Control. Fusion* **52** 075005

[5] Suttrop W. *et al* 1997 Identification of plasma-edge-related operational regime boundaries and the effect of edge instability on confinement in ASDEX Upgrade *Plasma Phys. Control. Fusion* **39** 2051–66

[6] Hubbard A.E., Boivin R.L., Drake J.F., Greenwald M., In Y., Irby J.H., Rogers B.N. and Snipes J.A. 1998 Local variables affecting h-mode threshold on alcator c-mod *Plasma Phys. Control. Fusion* **40** 689–92

[7] Burrell K.H. *et al* 1990 Physics of the L to H transition in the DIII-D tokamak *Phys. Fluids B-Plasma Phys.* **2** 1405–10

[8] Rogers B.N. and Drake J.F. 1997 Enhancement of turbulence in tokamaks by magnetic fluctuations *Phys. Rev. Lett.* **79** 229–32

[9] Burrell K.H. 1997 Effects of $E \times B$ velocity shear and magnetic shear on turbulence and transport in magnetic confinement devices *Phys. Plasmas* **4** 1499–518

[10] Connor J.W. and Wilson H.R. 2000 A review of theories of the l-h transition *Plasma Phys. Control. Fusion* **42** R1–R74

[11] Burrell K.H. *et al* 1992 Physics of the l-mode to h-mode transition in tokamaks *Plasma Phys. Control. Fusion* **34** 1859

[12] Sauter O. *et al* 2014 On the non-stiffness of edge transport in l-mode tokamak plasmas *Phys. Plasmas* **21** 055906

[13] Bourdelle C., Garbet X., Singh R. and Schmitz L. 2012 *Plasma Phys. Control. Fusion* **54** 115003

[14] Bourdelle C. *et al* 2014 L to h mode transition: on the role of z eff *Nucl. Fusion* **54** 022001

[15] Maggi C.F. *et al* 2014 L-h power threshold studies in jet with be/w and c wall *Nucl. Fusion* **54** 023007

[16] Sauter P. *et al* 2012 L- to h-mode transitions at low density in asdex upgrade *Nucl. Fusion* **52** 012001

[17] Schmitz L., Zeng L., Rhodes T.L., Hillesheim J.C., Doyle E.J., Groebner R.J., Peebles W.A., Burrell K.H. and Wang G. 2012 Role of zonal flow predator-prey oscillations in triggering the transition to h-mode confinement *Phys. Rev. Lett.* **108** 155002

[18] Tynan G.R. *et al* 2013 Turbulent-driven low-frequency sheared $E \times B$ flows as the trigger for the h-mode transition *Nucl. Fusion* **53** 073053

[19] Kobayashi T. *et al* 2013 Spatiotemporal structures of edge limit-cycle oscillation before l-to-h transition in the jft-2m tokamak *Phys. Rev. Lett.* **111** 035002

[20] Righi E., Campbell D.J., Conway G.D., Hawkes N.C., Horton L.D., Maggi C.F., Saibene G., Sartori R. and Zastrow K.D. 2000 Comparison between experimental and theoretical conditions for the L-H transition in JET *Plasma Phys. Control. Fusion* **42** A199–204

[21] Righi E. *et al* 1999 Isotope scaling of the h mode power threshold on jet *Nucl. Fusion* **39** 309

[22] Neu R. *et al* 2013 *J. Nucl. Mater.* **438** S34–41

[23] Ryter F. *et al* 2013 Survey of the H-mode power threshold and transition physics studies in ASDEX Upgrade *Nucl. Fusion* **53** 113003

[24] Horton L.D. *et al* 1999 Studies in JET diverters of varied geometry. I: non-seeded plasma operation *Nucl. Fusion* **39** 1–17

[25] Andrew Y. *et al* 2004 *Plasma Phys. Control. Fusion* **46** A87

[26] Fukuda T., Takizuka T., Tsuchiya K., Kamada Y. and Asakura N. 2000 Reduction of l-h transition threshold power under the w-shaped pumped divertor geometry in jt-60u *Plasma Phys. Control. Fusion* **42** A289

[27] Ma Y., Hughes J.W., Hubbard A.E., LaBombard B., Churchill R.M., Golfinopolous T., Tsujii N. and Marmar E.S. 2012 Scaling of h-mode threshold power and l-h edge conditions with favourable ion grad- b drift in alcator c-mod tokamak *Nucl. Fusion* **52** 023010

[28] Gohil P., Evans T.E., Fenstermacher M.E., Ferron J.R., Osborne T.H., Park J.M., Schmitz O., Scoville J.T. and Unterberg E.A. 2011 *Nucl. Fusion* **51** 103020

[29] Andrew Y. *et al* 2008 H-mode access on jet and implications for iter *Plasma Phys. Control. Fusion* **50** 124053

[30] Loarte A. 2001 Effects of divertor geometry on tokamak plasmas *Plasma Phys. Control. Fusion* **43** R183

[31] Guo H.Y. *et al* 2000 Effects of divertor geometry and chemical sputtering on impurity behaviour and plasma performance in JET *Nucl. Fusion* **40** 379–96

[32] McCracken G.M. *et al* 1999 Studies in JET diverters of varied geometry. III: intrinsic impurity behaviour *Nucl. Fusion* **39** 41–60

[33] Maggi C.F. *et al* 2014 *41st EPS Conf. on Controlled Fusion and Plasma Physics (Berlin, Germany, 23--27 June 2014)* http://ocs.ciemat.es/EPS2014PAP

[34] LaBombard B. *et al* 2005 Transport-driven scrape-off layer flows and the x-point dependence of the l-h power threshold in alcator c-mod *Phys. Plasmas* **12** 056111

[35] Jenko F., Dorland W., Kotschenreuther M. and Rogers B.N. 2000 Electron temperature gradient driven turbulence *Phys. Plasmas* **7** 1904–10

[36] Waltz R.E., Staebler G.M., Dorland W., Hammett G.W., Kotschenreuther M. and Konings J.A. 1997 A gyro-Landau-fluid transport model *Phys. Plasmas* **4** 2482–96

[37] Bourdelle C., Hoang G.T., Litaudon X., Roach C.M., Tala T., ITPA Topical Grp Transport ITB Phy and Int ITB Database Working Grp 2005 Impact of the alpha parameter on the microstability of internal transport barriers *Nucl. Fusion* **45** 110–30

[38] Edery D., Garbet X., Roubin J.P. and Samain A. 1992 Variational formalism for kinetic-mhd instabilities in tokamaks *Plasma Phys. Control. Fusion* **34** 1089–112

[39] Zonca F. *et al* 2007 Electron fishbones: theory and experimental evidence *Nucl. Fusion* **47** 1588

[40] Cottier P., Bourdelle C., Camenen Y., Gürcan Ö.D., Casson F.J., Garbet X., Hennequin P. and Tala T. 2014 Angular momentum transport modeling: achievements of a gyrokinetic quasi-linear approach *Plasma Phys. Control. Fusion* **56** 015011

[41] Romanelli M. *et al* 2007 Parametric dependence of turbulent particle transport in high density electron heated ftu plasmas *Plasma Phys. Control. Fusion* **49** 935–46

[42] Viezzer E. *et al* 2013 High-accuracy characterization of the edge radial electric field at asdex upgrade *Nucl. Fusion* **53** 053005

[43] Viezzer E., Pütterich T., McDermott R.M., Conway G.D., Cavedon M., Dunne M.G., Dux R., Wolfrum E. and the ASDEX Upgrade Team 2014 Parameter dependence of the radial electric field in the edge pedestal of hydrogen, deuterium and helium plasmas *Plasma Phys. Control. Fusion* **56** 075018

[44] Viezzer E., Pütterich T., Angioni C., Bergmann A., Dux R., Fable E., McDermott R.M., Stroth U., Wolfrum E. and the ASDEX Upgrade Team 2014 Evidence for the neoclassical nature of the radial electric field in the edge transport barrier of asdex upgrade *Nucl. Fusion* **54** 012003

[45] Ryter F., Barrera Orte L., Kurzan B., McDermott R.M., Tardini G., Viezzer E., Bernert M., Fischer R. and The ASDEX Upgrade Team 2014 Experimental evidence for the key role of the ion heat channel in the physics of the l-h transition *Nucl. Fusion* **54** 083003

[46] Staebler G. *et al* 2014 *42nd EPS Conf. on Controlled Fusion and Plasma Physics (Berlin, Germany, 23--27 June 2014)* http://ocs.ciemat.es/EPS2014PAP

[47] Chankin A.V. *et al* 2007 Discrepancy between modelled and measured radial electric fields in the scrape-off layer of divertor tokamaks: a challenge for 2d fluid codes? *Nucl. Fusion* **47** 479

[48] Loizu J., Ricci P., Halpern F.D., Jolliet S. and Mosetto A. 2013 On the electrostatic potential in the scrape-off layer of magnetic confinement devices *Plasma Phys. Control. Fusion* **55** 124019

[49] Delabie E. *et al* 2014 Overview and interpretation of lh threshold experiments on jet with the iter-like wall *Paper*

Presented at 25th IAEA Int. Conf. on Fusion Energy (St Petersburg, Russian, 13–18 October 2014) http://www-naweb.iaea.org/napc/physics/FEC/FEC2014/index.htm

[50] Hinton F.L. and Hazeltine R.D. 1976 Theory of plasma transport in toroidal confinement systems *Rev. Mod. Phys.* **48** 239–308

[51] Kim Y.B., Diamond P.H. and Groebner R.J. 1991 Neoclassical poloidal and toroidal rotation in tokamaks *Phys. Fluids B: Plasma Phys.* **3** 2050–60

[52] Tamain P., Bufferand H., Ciraolo G., Colin C., Ghendrih P., Schwander F. and Serre E. 2014 3D properties of edge turbulent transport in full-torus simulations and their impact on poloidal asymmetries *Contrib. Plasma Phys.* **54** 555–9

[53] Umansky M.V., Xu X.Q., Dudson B., LoDestro L.L. and Myra J.R. 2009 Status and verification of edge plasma turbulence code {BOUT} *Comput. Phys. Commun.* **180** 887–903

[54] Carlstrom T.N., Groebner R.J., Fenzi C., McKee G.R., Moyer R.A. and Rhodes T.L. 2002 Evidence for the role of velocity shear on the l-h transition in diii-d *Plasma Phys. Control. Fusion* **44** A333

[55] Fedorczak N., Diamond P.H., Tynan G. and Manz P. 2012 Shear-induced reynolds stress at the edge of l-mode tokamak plasmas *Nucl. Fusion* **52** 103013

[56] Stangeby P. 2000 *The Plasma Boundary of Magnetic Fusion Devices Bristol: Institute of Physics Publishing*

[57] Gohil P. *et al* 2012 Assessment of the h-mode power threshold requirements for iter *Proc. 24th Int. Conf. on Fusion Energy (San Diego, USA, 8–13 October 2012)* http://www-naweb.iaea.org/napc/physics/FEC/FEC2012/index.htm

[58] McDonald D.C. *et al* 2010 Jet helium-4 elmy h-mode studies *Fusion Energy Proc. 23rd Int. Conf. Daejeon (Daejeon, Korea, 11–16 October 2010)* (Vienna: IAEA) http://www-naweb.iaea.org/napc/physics/FEC/FEC2010/index.htm

[59] Chôné L., Beyer P., Sarazin Y., Fuhr G., Bourdelle C. and Benkadda S. 2014 *Phys. Plasmas* **21** 070702

[60] Park G.Y., Kim S.S., Jhang H., Diamond P.H., Rhee T. and Xu X.Q. 2015 Flux-driven simulations of turbulence collapse *Phys. Plasmas* **22** 032505